Evaluation of various approximations used in the envelope-function method

A. T. Meney and Besire Gonul
Department of Physics, University of Surrey, Guildford, Surrey GU2 5XH, United Kingdom

E. P. O'Reilly*
Fraunhofer-Institut für Angewandte Festkörperphysik, Tullastrasse 72, D-79108 Freiburg, Federal Republic of Germany
(Received 16 May 1994; revised manuscript received 6 July 1994)

We investigate a number of issues related to the application of the envelope-function method to calculate confined-state energies and subband structure in quantum-well structures. We first consider zone-center confined-state energies and show how the explicit elimination of spurious solutions from the envelope-function band structure leads to a slightly modified form of the standard result through which the conduction-band confined-state energies are calculated using a one-band model and an energy-dependent effective mass. We show that the effects of nonparabolicity can be predicted directly from the bulk band structure in an infinitely deep quantum well, and demonstrate how the bulk band structure can also be used to predict the errors in calculated confinement energies in wells of finite depth. The correct choice of boundary conditions still remains controversial for the calculation of valence-subband structure using the Luttinger-Kohn Hamiltonian. We compare the valence-band structure calculated with the lowest conduction band included either explicitly or treated as a remote band, using perturbation theory. We demonstrate that the boundary conditions recently derived by Burt and Foreman are correct. Finally, we compare the valence-band structure calculated using the 4×4 and 6×6 Luttinger-Kohn Hamiltonians. We show how the warping of the highest valence band is markedly different at both intermediate and large wave vectors when the spin-split-off band is included. The use of the axial model to calculate valence-band density of states is therefore questionable with the 6×6 Hamiltonian. The calculated warping is very sensitive to the values of the Luttinger γ parameters used, indicating the importance of investing more effort to determine these parameters accurately.

I. INTRODUCTION

The envelope-function method is widely used to calculate confined-state energies and subband structure in the lowest conduction and highest valence bands of III-V and other semiconductor systems.[1–4] There are several different formulations of the envelope-function method, each differing in terms of the number of bulk bands which are included and the boundary conditions which are used to describe the continuity of the envelope functions across the interfaces between different materials. An overview of these different formulations is provided in the recent paper by Winkler and Rössler.[5] The most general form of the envelope-function method used in the literature includes the lowest conduction band and the three highest valence bands, namely the heavy-hole, light-hole, and spin-split-off bands.[6–13] When electron spin is included, these bands are doubly degenerate at the zone center, so that a total of eight bands are then included in the general model. Calculations using this eight-band model are difficult, due in particular to the presence of spurious solutions.[5,6] As a result, most calculations generally invoke a number of simplifications, for instance by including only heavy-hole, light-hole, and split-off bands,[14–16] or often only the heavy- and light-hole bands.[17–22] The results obtained vary according to the prescription used, but there are few guidelines given in the literature as to how to choose an appropriate model for a given problem. We demonstrate here that the accuracy of the calculated zone-center energies and subband dispersions can be predicted by plotting the equivalent bulk band structure under various approximations.

A number of authors have derived how conduction-band confined-state energies can be accurately calculated in semiconductor quantum wells (QW's) by using a one-band model with an energy-dependent effective mass.[6,23–27] We present here an alternative derivation of this result which explicitly considers the role of spurious solutions in the band structure, and then use this result to make a number of general comments on the influence of nonparabolicity on confined-state energies.

There are a number of formulations of the boundary conditions describing the variation of the envelope function across an interface. The most widely used approach assumes a "symmetrized" form of the Hamiltonian.[28–32] Burt has recently presented an exact derivation of envelope-function theory,[4] whose specific form for the boundary conditions is different to the conventional conditions. Foreman has derived explicitly the form of the Burt boundary conditions for the valence-band Hamiltonian and presented a relatively subtle example from the $GaAs/Al_xGa_{1-x}As$ material system, which suggests that it is most appropriate to use the Burt boundary conditions.[33] We present a more direct example here, by comparing the valence-band structure calculated with and without inclusion of the conduction band in the calcula-

tion, and demonstrate that the Burt boundary conditions give the more physically plausible results.

We also investigate the influence of the spin-split-off band on valence-subband dispersion, and find that its effects are much stronger than would be expected by just considering its influence on calculated zone-center confined-state energies. Further, the calculated subband dispersion when the split-off band is included is particularly sensitive to an input parameter which is not always well known, namely the difference between the Luttinger γ_2 and γ_3 values used in the valence-band Hamiltonian.

We begin in Sec. II by presenting the envelope-function Hamiltonian. We demonstrate that the effects of nonparabolicity on zone-center confined-state energies can be predicted directly from the bulk band structure for an infinitely deep quantum-well structure. In Sec. III, we rederive the standard one-band expression for conduction-band confined-state energies, emphasizing the elimination of contributions from spurious bands. We then use this expression to make general comments concerning the effects of nonparabolicity on zone-center confined-state energies in finite quantum-well structures, and present calculations which support our conclusions. We illustrate in Sec. IV the effects of different boundary conditions on the calculated subband dispersion in the quantum-well plane, and consider also the influence of the spin-split-off band. Finally we summarize our conclusions in Sec. V.

II. ENVELOPE-FUNCTION HAMILTONIAN

The envelope-function approach can be viewed as a generalization of Kane's $\mathbf{k}\cdot\mathbf{p}$ method to describe semiconductor heterostructures.[34] The second-order bulk eight-band Hamiltonian quantized along the z direction is given using the same basis states as in Ref. 11 by

$$H=\begin{bmatrix} E_{\rm CB} & -\sqrt{3}T_+ & \sqrt{2}U & -U & 0 & 0 & -T_- & -\sqrt{2}T_- \\ & E_{\rm HH} & \sqrt{2}L & -L & 0 & 0 & -R & -\sqrt{2}R \\ & & E_{\rm LH} & Q & T_+^* & R & 0 & \sqrt{3}L \\ & & & E_{\rm SO} & \sqrt{2}T_+^* & \sqrt{2}R & -\sqrt{3}L & 0 \\ & & & & E_{\rm CB} & -\sqrt{3}T_- & \sqrt{2}U & -U \\ & & & & & E_{\rm HH} & \sqrt{2}L^* & -L^* \\ & & & & & & E_{\rm LH} & Q \\ & & & & & & & E_{\rm SO} \end{bmatrix}, \tag{1}$$

where the subscripts CB, HH, LH, and SO stand for the conduction, heavy-hole, light-hole, and split-off bands, respectively, and

$$E_{\rm CB}=E_{c0}+\tfrac{1}{2}s(k_t^2+k_z^2)\ ,$$
$$E_{\rm HH}=E_{v0}-\tfrac{1}{2}(\gamma_1-2\gamma_2)k_z^2-\tfrac{1}{2}(\gamma_1+\gamma_2)k_t^2\ ,$$
$$E_{\rm LH}=E_{v0}-\tfrac{1}{2}(\gamma_1+2\gamma_2)k_z^2-\tfrac{1}{2}(\gamma_1-\gamma_2)k_t^2\ ,$$
$$E_{\rm SO}=E_{v0}-\Delta_0-\tfrac{1}{2}\gamma_1k_z^2-\tfrac{1}{2}\gamma_1k_t^2\ ,$$
$$T_\pm=(1/\sqrt{6})Pk_\pm\ ,$$
$$U=(1/\sqrt{3})Pk_z\ ,$$
$$L=(\sqrt{3/2})\gamma_3k_zk_-\ ,$$
$$R=(\sqrt{3}/2)(\gamma_{\rm av}k_-^2-\mu k_+^2)\ ,$$
$$Q=\sqrt{2}\gamma_2k_z^2-(1/\sqrt{2})\gamma_2k_t^2\ ,$$
$$k_\pm=k_x\pm ik_y,\quad k_t^2=k_x^2+k_y^2\ ,$$
$$\gamma_{\rm av}=\tfrac{1}{2}(\gamma_2+\gamma_3),\quad \mu=\tfrac{1}{2}(\gamma_3-\gamma_2)\ ,$$

where E_{c0} and E_{v0} are the Γ-point conduction- and valence-band-edge energies, Δ_0 is the magnitude of the spin-orbit splitting at $k=0$, and P is the Kane matrix element.[34] We have taken $\hbar=m=1$. The lower triangular matrix elements (not shown) are obtained by Hermitian conjugation. The parameters γ_i are related to the valence-band Luttinger parameters γ_i^L by the relations[35]

$$\gamma_1^L=\gamma_1+E_p/(3E_g)\ ,$$
$$\gamma_2^L=\gamma_2+E_p/(6E_g)\ , \tag{2}$$
$$\gamma_3^L=\gamma_3+E_p/(6E_g)\ ,$$

where E_g is the fundamental band gap and E_p is related to the Kane matrix element P by $E_p=2mP^2/\hbar^2$. The coupling between the conduction and valence bands is explicitly included in the eight-band model, and the value of the parameter s in the $E_{\rm CB}$ is then obtained from the experimentally determined conduction-band mass m_c^* using

$$m_c^{*-1}=s+\frac{E_p}{3}\left[\frac{2}{E_g}+\frac{1}{E_g+\Delta_0}\right]. \tag{3}$$

In the six-band model comprising the CB, HH, and LH bands, we replace s by s', where

$$s'=m_c^{*-1}-\frac{2}{3}\frac{E_p}{E_g}\ , \tag{4}$$

so that we indirectly maintain the contribution of the spin-split-off band to the conduction-band effective mass. In the 4×4 and 6×6 Luttinger models, we replace the parameters γ_i by γ_i^L in Eq. (1), and neglect coupling to (i) the conduction band in the 6×6 model and (ii) the conduction and split-off bands in the 4×4 model. In both of these models we use a parabolic approximation for the conduction band, since this represents the conduction-band dispersion to exactly the same order as the Luttinger model represents the valence-band dispersion. It should be noted that one advantage of the eight-band model is that it treats equally all of the bands explicitly included in the calculation.

To obtain the matrix eigenvalue equation for quantum-well (or superlattice) subband dispersion, we include the explicit z dependence of the band-edge energies, E_{c0}, E_{v0}, and Δ_0, and the effective-mass parameters s and γ_i which appear in Eq. (1). Taking growth to be along the (001) direction, we replace k_z by the operator $-i\partial/\partial z$, and include the valence-band-edge offset at each interface, either using an experimental result or a theoretical estimate obtained, for example, by using the model solid theory of Van de Walle.[36] We assume similar values for the parameter P in each layer, and utilize the value corresponding to the material in the QW, although this is not a necessary assumption.[37]

In order to simplify the problem as far as possible, it is common to block diagonalize the eight-band Hamiltonian. We do this following the method outlined in Ref. 11. We first ignore the warping part of the Hamiltonian (terms involving μ) and obtain a unitary transformation which block diagonalizes the remaining terms. The same transformation is then applied to the warping terms. Although not exact, the resulting 4×4 Hamiltonians approximate well the correct in-plane warping of the full 8×8 Hamiltonian in a similar fashion to the Broido-Sham transformation of the 4×4 Luttinger Hamiltonian.[19] Note, however, that the dispersion is in fact exact for certain in-plane angles, namely $\theta=n\pi/4$ ($n=0,1,2,\ldots$). The resulting transformed matrix is then represented by

$$U^{\dagger}HU=\begin{bmatrix} H_u & H_{ul} \\ H_{lu} & H_l \end{bmatrix}, \tag{5}$$

where the H_n are 4×4 block matrices, and $H_{lu}=H_{ul}^{\dagger}$. The upper-left 4×4 block is given by

$$H_u=\begin{bmatrix} E_c & P_1 & P_2 & P_3 \\ P_1^* & E_{\rm HH} & A & B \\ P_2^* & A^* & E_{\rm LH} & C \\ P_3^* & B^* & C^* & E_{\rm SO} \end{bmatrix}, \tag{6}$$

where

$$P_1=-(1/\sqrt{2})Pk_{\parallel}$$

$$P_2=(\sqrt{2}/\sqrt{3})Pk_z+(i/\sqrt{6})Pk_{\parallel} ,$$

$$P_3=-(1/\sqrt{3})Pk_z+(i/\sqrt{3})Pk_{\parallel} ,$$

$$A=\sqrt{3}\gamma_3 k_{\parallel}k_z+i(\sqrt{3}/2)\gamma(\theta)k_{\parallel}^2 ,$$

$$B=-(\sqrt{3}/\sqrt{2})\gamma_3 k_{\parallel}k_z+i(\sqrt{3}/\sqrt{2})\gamma(\theta)k_{\parallel}^2 ,$$

$$C=\sqrt{2}\gamma_2 k_z^2-(1/\sqrt{2})\gamma_2 k_{\parallel}^2-i(3/\sqrt{2})\gamma_3 k_{\parallel}k_z ,$$

$$k_{\parallel}^2=k_x^2+k_y^2,\quad \gamma(\theta)=\gamma_{\rm av}-\mu\cos(4\theta) ,$$

$$\theta=\tan^{-1}(k_y/k_x) .$$

We can obtain H_1 from H_u by replacing $k_{\parallel}$ with $-k_{\parallel}$. The warping terms in the 8×8 Hamiltonian which are not fully diagonalized by this transformation are given by the cross matrix

$$H_{ul}=\begin{bmatrix} 0 & 0 & 0 & 0 \\ 0 & 0 & -\alpha & -\alpha \\ 0 & \alpha & 0 & 0 \\ 0 & \alpha & 0 & 0 \end{bmatrix}, \tag{7}$$

where

$$\alpha=(\sqrt{3}/2)\mu k_{\parallel}^2\sin(4\theta) . \tag{8}$$

The α terms then vanish at the zone center and increase as the in-plane wave vector squared, so that the effect of ignoring them is only significant at large values of in-plane momentum $k_{\parallel}$. Further, we choose here to solve H_u along k_x for which the term α is zero, so the results presented below are identical to those which would be obtained using the full eight-band model.

We consider below four different models based on the Hamiltonian of Eq. (6), namely (i) the four-band model, with coupled CB, HH, LH, and SO bands; (ii) a two-band model, with coupled HH and LH, and parabolic CB, with the split-off band neglected; (iii) a mixed three-band model, with coupled CB, HH, and LH, and neglecting the SO band; and (iv) a three-valence-band model, with coupled HH, LH, and SO, and parabolic CB. In models (i) and (iii), we use the valence-band effective-mass parameters γ_i, whereas in (ii) and (iv) we use instead the Luttinger parameters γ_i^L. These two sets of γ parameters are related by Eq. (2). Additionally, the conduction-band effective-mass parameter is given by s in model (i), while it is obtained from Eq. (4) in model (iii).

III. INFINITE WELL HAMILTONIAN

In this section, we apply the envelope-function Hamiltonian of Eq. (6) to demonstrate that the zone-center confined-state energies in an infinitely deep quantum well can be determined directly from a plot of the bulk band dispersion along the growth direction. At the center of the two-dimensional Brillouin zone, where $k_{\parallel}=0$, Eq. (6) decouples into two independent matrices, a 1×1 matrix describing the heavy-hole dispersion and a 3×3 matrix, which needs to be solved to calculate the (mixed) CB, LH, and SO confined-state energies.

Because of this decoupling, the heavy-hole zone-center confined-state energies are identical in the four models considered above. If we take $E_{v0}=0$, the heavy-hole bulk dispersion along k_z is given by

$$E_{HH}(k_z) = -\tfrac{1}{2}(\gamma_1 - 2\gamma_2)k_z^2 \ . \tag{9}$$

If we define the quantum well between $z=0$ and L, and apply the boundary conditions that the envelope function $f(z)$ goes to zero at the interfaces,[4] we find that the heavy-hole confined states are standing waves with wave vector $k_z = n\pi/L$. The envelope functions are given by

$$f_n(z) = (\sqrt{2}/\sqrt{L})\sin(n\pi z/L), \quad 0 < z < L$$
$$= 0 \quad \text{otherwise} \ , \tag{10}$$

and the confined-state energies are found directly from the bulk band structure by replacing k_z by $n\pi/L$ in Eq. (9).

We can solve the remaining 3×3 matrix using an expansion in diagonal (uncoupled) states.[22,38] We consider the calculation of a confined-state predominantly of light-hole character, for which the light-hole component of the envelope function varies as $f_{LHm}(z) = \sin(m\pi z/L)$. If we allow the split-off component of the wave function also to vary as $f_{SOp}(z) = \sin(p\pi z/L)$, then the off-diagonal term involving k_z^2 introduces a direct mixing between normalized light-hole and split-off components such that[38]

$$\langle f_{SOp}(z)| -\partial^2/\partial z^2 | f_{LHm}(z)\rangle = (m\pi/L)^2\delta_{pm} \ , \tag{11}$$

i.e., the only direct mixing between f_{LHm} and the split-off band is with f_{SOm}, and the magnitude of the interaction is found by replacing k_z^2 by $(m\pi/L)^2$ in the 3×3 matrix. Finally, the terms P_2 and P_3 linking the conduction band to the light-hole and split-off bands are both of order k_z. The correct form for the conduction-band contribution to the envelope function is $f_{CBq}(z) = i\cos(q\pi z/L)$, so that f_{LHm} and f_{SOm} mix only with the conduction-band component f_{CBm}, with the magnitude of the interaction found by replacing k_z in $P_{2,3}$ by $m\pi/L$ in Eq. (6). Hence, the zone-center energy of the mth LH, SO, and CB confined states in an infinite quantum well can be found by replacing each occurrence of k_z in Eq. (6) with $m\pi/L$.

The zone-center confined-state energies in an infinite well of width L are then just equal to the bulk band energies at $k_z = m\pi/L$ for each of the four calculation models described at the end of Sec. II. We thus conclude that in an infinite well the difference between calculated confined-state energies using different models can be predicted directly from the differences in the bulk band structures. We consider in Sec. IV how this conclusion is modified in the case of finite wells.

IV. ZONE-CENTER CONFINED-STATE ENERGIES

A. Analytic results

A number of authors have demonstrated that the even confined-state energies for a nonparabolic conduction band can be calculated accurately using the expression[6,23,27]

$$k_z \frac{E}{k_z^2}\tan(k_z a) = \kappa_z \frac{V_0 - E}{\kappa_z^2} \ , \tag{12}$$

where the well is defined between $z = \pm a$, the zero of energy is taken at the conduction-band minimum in the well, and the conduction-band offset is set equal to V_0. The band structure varies as $E_w(k_z)$ in the well, while the evanescent band in the barrier band-gap region varies as $E_b(\kappa_z)$. For parabolic bands, Eq. (12) reduces to the well-known form

$$\frac{k_z}{m_w^*}\tan(k_z a) = \frac{\kappa_z}{m_b^*} \ . \tag{12a}$$

A similar expression to Eq. (12) can also be used for odd states, with $\tan(k_z a)$ replaced by $-\cot(k_z a)$. This single-band expression has the advantage that it avoids any reference to or use of spurious solutions to the band structure which can otherwise be found in the full envelope-function method. The elimination of spurious solutions is often a concern in applications of the multiband envelope-function method.[5,6,8] We consider here a two-band Hamiltonian, including a spurious band at large wave vector, and show how forced elimination of the spurious bands from the allowed solutions does indeed lead to an expression similar but not exactly identical to Eq. (12) for confined conduction states. We then apply the one-band expression to analyze the effects of band nonparabolicity on confined-state energies.

We consider a two-band Hamiltonian which for $k_\parallel = 0$ takes the form

$$H = \begin{bmatrix} -dk_z^2 & iPk_z \\ -iPk_z & -E_g - bk_z^2 \end{bmatrix} . \tag{13}$$

This expression represents a single conduction band interacting with a single valence band. Equation (6) reduces to this form for $k_\parallel = 0$ in the case where the spin-orbit splitting Δ_0 tends either to zero or infinity. The bulk band structure of Eq. (13) is plotted schematically in Fig. 1 for the case where $b, d > 0$. It can be seen that for small values of k the band dispersion does indeed mimic that of a direct-gap semiconductor, but at large k the on-diagonal terms in k^2 start to dominate, giving a second, spurious state at each energy E in the neighborhood of the band gap. The spurious solutions arise due to the inclusion of the two terms of order k_z^2 in Eq. (13):

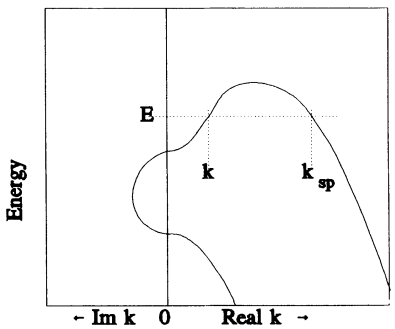

FIG. 1. Schematic band structure of the two-band Hamiltonian of Eq. (13). Two eigenstates are found at each energy E, the second of which (with wave vector k_{sp}) is a spurious solution.

when $bd>0$, the spurious band is at large, real wave vector, as in Fig. 1; if we had chosen $bd<0$, we would still have obtained a spurious band, but in this case at large imaginary wave vector in the neighborhood of the band gap. We wish to eliminate the contribution of these spurious states in quantum-well calculations.

Equation (13) is of the form

$$Hf=Ef \ ,$$

where

$$Hf=A\,d^2f/dz^2+B\,df/dz+Cf \ . \tag{14}$$

We see from Fig. 1 that at each energy of interest E, there are two allowed k values in the well, k and k_{sp} (see Fig. 1), as also in the barrier, κ and k_{sb}. We can calculate the envelope function associated with each state at energy E, and find for even states in a symmetric quantum well that the general even solutions vary as

$$f(z)=x_1\begin{bmatrix}\cos kz\\ \dfrac{E+d_wk^2}{Pk}\sin kz\end{bmatrix}+x_2\begin{bmatrix}\cos k_{sp}z\\ \dfrac{E+d_wk_{sp}^2}{Pk_{sp}}\sin k_{sp}z\end{bmatrix} \tag{15}$$

while in the barrier we have

$$f(z)=y_1\exp(-\kappa z)\begin{bmatrix}1\\ \dfrac{V_0-E+d_b\kappa^2}{P\kappa}\end{bmatrix}+y_2\begin{bmatrix}\cos k_{sb}z\\ \dfrac{E+d_bk_{sb}^2-V_0}{Pk_{sb}}\sin k_{sb}z\end{bmatrix} \ . \tag{16}$$

The two-component envelope functions must satisfy the boundary conditions[13]

$$f \text{ continuous} \tag{17a}$$

$$A\,df/dz+\tfrac{1}{2}Bf \text{ continuous} \ . \tag{17b}$$

We have four unknown quantities in Eqs. (15) and (16) and, from Eq. (17), four boundary conditions for even solutions of the envelope-function equation. We can, however, in principle add two further boundary conditions for acceptable solutions to the Hamiltonian, namely that $x_2=y_2=0$, so that there is no contribution from the spurious bands. We adopt these two boundary conditions, so that Eq. (17) then leaves us with four boundary conditions for the two unknown quantities x_1 and y_1. As we are considering confined electron states, we choose to solve the upper (conduction band) components of Eqs. (17a) and (17b) exactly. We find for even solutions that

$$k\frac{E-d_wk^2}{k^2}\tan ka=\kappa\frac{V_0-E-d_b\kappa^2}{\kappa^2} \ . \tag{18}$$

This expression is similar, but not identical to, Eq. (12), as it contains extra terms involving d_wk^2 and $d_b\kappa^2$. However, the dominant contribution to the zone-center conduction-band dispersion in the direct-gap III-V semiconductors comes from the off-diagonal interactions of order k, rather than these smaller on-diagonal elements of order k^2. Also, although the conduction-band dispersion is most accurately described using a multiband Hamiltonian, it can usually be well approximated by a two-band Hamiltonian such as Eq. (13).[39] Equations (12) and (18) should give very similar eigenvalues for the III-V heterostructures considered here. We therefore now apply the previously derived Eq. (12) to analyze the effects of band nonparabolicity on electron confined-state energies.

Consider first an infinite square well. In this case $\kappa=\infty$, so that the right-hand side of Eq. (12) is infinite. We therefore require that the left-hand side is also infinite, so that for symmetric confined states we have $ka=\pi/2+n\pi$, as also derived in Sec. III using the multiband Hamiltonian.

In a finite square well with parabolic bands, the terms E/k^2 and $(V_0-E)/\kappa^2$ in Eq. (12) are independent of energy and proportional to the inverse effective mass in the well and barrier, respectively. For $k=0$, the left-hand side of Eq. (12) is always smaller than the right-hand side, and the ground state is then found by increasing the value of k until the two sides are equal. When band nonparabolicity is considered, E/k^2 decreases with increasing E, while $(V_0-E)/\kappa^2$ increases with E. The ground state in the nonparabolic finite well case will therefore always have a larger wave vector k associated with it than in the equivalent parabolic band model, as previously discussed by Nelson, Miller, and Kleinman.[39] We provide examples below which show that the ground-state confinement energy with nonparabolic bands remains smaller than the parabolic case in deep wells, but can in other instances be even larger than in the parabolic band case, due to a significant increase in the ground-state value of k.

For higher confined states, we can apply a similar argument to show that the k vector in the nonparabolic model, k_{np}, remains larger than in the parabolic model, k_p. However the difference between k_{np} and k_p decreases rapidly with increasing excited-state index. The following argument indicates why this is so. Let k be the wave vector in the well describing the ground-state solution to the envelope-function equation for a well of width $2a$. We see by substitution in Eq. (12) that the same value of k will describe an excited-state solution for a well of width $2b$, so long as

$$kb=ka+n\pi/2 \ , \tag{19}$$

i.e., so long as

$$b=a+n\pi/2k \ . \tag{20}$$

As $k_{np}>k_p$, the excited states for the given k values are then in narrower wells in the nonparabolic than in the parabolic model ($b_{np}<b_p$). Equivalently, for a fixed well width, we then expect the k vector for excited states in the nonparabolic model to approach (from above) that of the parabolic model, confirming the usual conclusion that nonparabolicity can have a greater influence on excited

state than ground-state confinement energies.[39]

A two-band model such as Eq. (13) is generally not so accurate for the determination of light-hold confined-state energies, as the light-hole nonparabolicity has significant contributions from two distinct bands, namely the conduction band and the split-off band. Nevertheless, we demonstrate below that the overall conclusions we derive concerning the influence of nonparabolicity on confined electron states are also applicable to light-hole states.

B. Numerical results

We have argued above that the accuracy of the calculated zone-center energies using different models can be predicted by plotting the equivalent bulk band structures. We present here the results of calculations which illustrate this point. We calculate the variation of confined-state energy with well width for two different material combinations: GaAs/AlAs, and then a lattice-matched $In_xGa_{1-x}AsSb/Al_yGa_{1-y}Sb$ structure, which illustrates the effects of strong nonparabolicity and of large spin-orbit splitting. The band-structure parameters used here and in later sections are listed in Table I. The Hamiltonian of Eq. (1) and the four models we are considering describe the band dispersion about the Brillouin-zone center, near the Γ point, so do not include Γ-X interactions. Thus, although the conduction-band minimum is near the X point in AlAs, we only examine here the confinement of Γ electrons in GaAs by the Γ well in AlAs. It is beyond the scope of the present paper to consider the incorporation of Γ-X interactions into the envelope-function method; such a modification is in principle possible,[4] but in most circumstances has little influence on calculated Γ well confinement energies.

Figure 2(a) illustrates the conduction-band structure of bulk GaAs calculated using models (i) (solid line, CB, LH, SO mixing at zone center), (ii) the parabolic band model (dotted line, CB only), and (iii), with coupled CB and LH (dashed line). The bulk band structures calculated using models (i) and (iii) are virtually identical up to about 200 meV above the band edge, and we find that the calculated confined-state energies for GaAs/AlAs quantum wells [Fig. 2(b)] are also in close agreement in this energy range. It can also be seen from Fig. 2(b) that the difference between the calculated parabolic and nonparabolic confinement energies increases with confined-state index, approaching the difference in bulk band energies

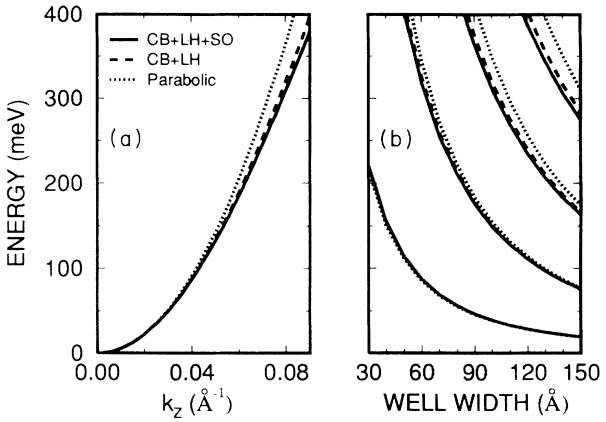

FIG. 2. (a) Conduction-band structure of bulk GaAs calculated along the (001) direction, using three different Hamiltonians, as described in text. (b) Electron confined-state energy as a function of well width in a GaAs/AlAs quantum well, using the three different Hamiltonians.

for the highest confined states. The ground-state confinement energy in the thinnest wells is higher in the nonparabolic models than in the parabolic case, even though $V_0 = 967$ meV here. We have confirmed by taking a very large conduction-band offset that the confinement energy in the nonparabolic models drops below the parabolic band value as one approaches an infinite square well.

Turning to the valence bands, Fig. 3(a) shows how the light-hole dispersion varies between the four different models, where we have now also included model (iv), with coupled LH and SO bands (dot-dashed line). We see that the interactions with both the conduction and split-off band increase the light-hole band nonparabolicity. This may initially appear surprising: the light-hole band is surrounded by the conduction band and the split-off band, so it might be expected from perturbation theory that the influence of these bands would balance each other. However, the zone-center interaction P_2 between the conduction and light-hole bands is of order k_z: this contributes in second-order perturbation theory to the parabolic (k_z^2) dispersion of the light-hole band; the subparabolic dispersion then arises from higher-order interactions. By contrast, the zone-center interaction C between the light-hole and split-off bands is of order k_z^2, which from second-order perturbation theory then leads to the

TABLE I. Material parameters used in the band-structure calculations (from Refs. 40 and 41).

	GaAs	AlAs	$Al_{0.2}Ga_{0.8}As$	$Al_{0.4}Ga_{0.6}Sb$	$In_{0.16}Ga_{0.84}As_{0.14}Sb_{0.86}$
m_c^*	0.0665	0.150	0.083	0.099	0.043
γ_1^L	6.85	3.45	5.644	6.70	12.65
γ_2^L	2.10	0.68	1.565	1.91	4.52
γ_3^L	2.90	1.29	2.318	2.89	5.61
E_g (meV)	1519	3130	1746	1239	626
Δ_0 (meV)	341	275	328	660	647
E_p (eV)	25.7	21.1	24.8	18.4	18.4
ΔE_c (meV)		967	136	520	
ΔE_v (meV)		644	91	94	

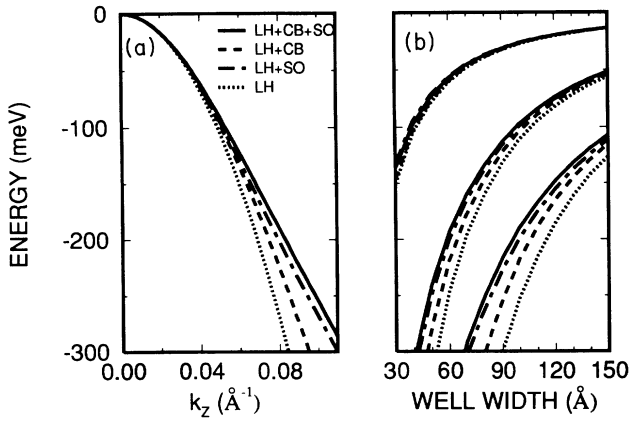

FIG. 3. (a) Dispersion of the light-hole band in bulk GaAs calculated along the (001) direction, using four different Hamiltonians, as described in text. (b) Energy of the light-hole states as a function of well width in a GaAs/AlAs quantum well, using the four Hamiltonians.

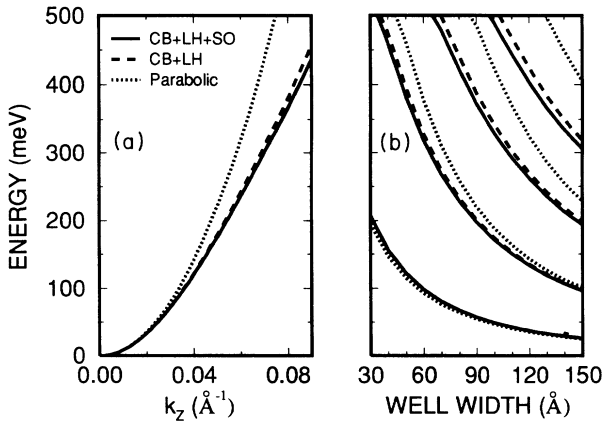

FIG. 4. (a) Conduction-band structure of bulk $In_{0.16}Ga_{0.84}As_{0.14}Sb_{0.86}$ calculated along the (001) direction using three different Hamiltonian models. (b) Electron confinement energy as a function of well width in $In_{0.16}Ga_{0.84}As_{0.14}Sb_{0.86}/Al_{0.4}Ga_{0.6}Sb$ quantum wells, using the three Hamiltonians.

observed repulsive interaction (initially of order k_z^4) between the light-hole and split-off bands.

We see in Fig. 3 how the strongest nonparabolicity is obtained in the two models which include the split-off band, and that the calculated confinement energies in these two cases always lie below those from the other two models. Even for the ground state, the calculated confinement energies are reduced in the nonparabolic models here compared to the parabolic case, although it is interesting to note that the ordering of the LH-CB-SO and LH-SO ground-state curves are reversed compared to that found in the bulk band structure. We again see how the difference between the calculated confined-state energies becomes more marked with increasing confined-state index. Overall, the differences between the various bulk band structures of Figs. 2(a) and 3(a) provide a good guide to the resulting differences in calculated confined-state energies.

Similar conclusions are obtained for the other materials systems which we have studied. Figure 4(a) shows the calculated conduction-band dispersion for a particular $In_xGa_{1-x}AsSb$ alloy lattice matched to GaSb. The nonparabolicity is now considerably stronger than in GaAs, and the energy of the lowest confined electron state increases by about 10 meV in the narrowest wells in the nonparabolic compared to the parabolic models [Fig. 4(b)]. The excited states, however, follow the same band ordering in the quantum well as in the bulk case, and it is again clear that the differences in the confined-state energies approach the differences in bulk band structures with increasing confined-state index.

Figure 5(a) shows the light-hole band dispersion for the same $In_xGa_{1-x}AsSb$ alloy as in Fig. 4. In this case, the dispersion curves are plotted over a smaller energy range than in the previous figures, because the valence-band offset relative to $Al_{0.4}Ga_{0.6}Sb$ is calculated to be only 94 meV. Due to the large spin-orbit splitting, a very similar band dispersion is found in models (i) (LH+CB+SO) and (iii) (LH+CB). We would thus predict that the calculated light-hole confinement energies should also be virtually identical in the two models, and this is indeed found to be the case [Fig. 5(b)].

Overall, we conclude from Figs. 2–5 that the accuracy of the calculated zone-center energies under different approximations can be well estimated by using the different models to plot the bulk band structure along the growth direction. We have only considered structures here where the zone-center electron and hole quantum wells are both in the same material layer, giving a type-I quantum well at the Γ point. We found in this case that we could ignore the behavior of the bands in the barrier layers. We expect, however, that for structures with type-II or other staggered Γ-band alignments, it would be necessary to consider the variation in band dispersion in each layer in order to identify the most appropriate Hamiltonian for the particular problem.

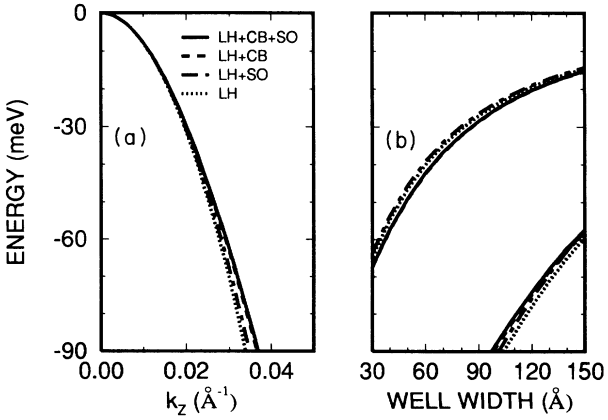

FIG. 5. (a) Dispersion of the light-hole band in bulk $In_{0.16}Ga_{0.84}As_{0.14}Sb_{0.86}$ calculated along the (001) direction using four different Hamiltonians. (b) Energy of the light-hole states as a function of well width in $In_{0.16}Ga_{0.84}As_{0.14}Sb_{0.86}/Al_{0.4}Ga_{0.6}Sb$ quantum wells, using the four Hamiltonians.

V. VALENCE-SUBBAND DISPERSION

While the effective-mass Hamiltonian of Eq. (6) has been widely used to study the valence-subband dispersion in quantum wells and heterostructures, the correct boundary conditions to connect the envelope functions across an abrupt interface still remain the subject of debate. Most authors have followed the approach of Altarelli and co-workers,[17,28] who argued that the envelope function and the probability current density must be continuous across each interface. When directly applied to Eq. (6), this leads to boundary conditions of the form of Eq. (17). Such an argument does not, however, provide the only possible set of boundary conditions. The main problem arises in choosing how to write terms like γk_z^2 or Pk_z when the scalar k_z is replaced by the operator $-i\partial/\partial z$. The Hamiltonian for instance remains Hermitian when γk_z^2 is replaced by $-\gamma^{\alpha}\partial/\partial z\gamma^{\beta}\partial/\partial z\gamma^{\alpha}$ so long as $2\alpha+\beta=1$, but the boundary conditions and hence calculated subband dispersion change as α and β are varied.[29–32]

Until recently, there was no *a priori* argument as to how the Hamiltonian should be modified to incorporate the operator $-i\partial/\partial z$. The situation has now changed with the development by Burt of an exact envelope-function theory for semiconductor microstructures.[4] This gives a general solution for the effective-mass Hamiltonian, which applies even at an abrupt interface. This theory can be applied to derive interface boundary conditions which then include correctly the effects of remote bands on the bulk dispersion and at the interfaces. Foreman[33] has applied Burt's prescription and derived a modified form of the valence-band part of the Hamiltonian in Eq. (6), treating the conduction band as a remote band. He then presented a relatively subtle example to support his boundary conditions, based on the behavior of the HH2 zone-center effective mass under different boundary conditions.

We present some more direct examples here, based on material systems similar to those discussed in Sec. IV which confirm that the Burt boundary conditions are the correct ones to use at heterostructure interfaces. We compare the valence-subband dispersion when we explicitly include the conduction band in the Hamiltonian and when we treat it as a remote band, using the standard symmetrized boundary conditions and the Foreman boundary conditions. The reader is referred to the paper by Foreman for the explicit form of the two sets of boundary conditions.[33] We keep the Kane matrix element P constant between the well and barrier material, so that it is then trivial to extend Foreman's three-band boundary conditions to the four-band case.

We also investigate a second issue, namely the influence of the spin-split-off band on the bulk valence-band structure, and hence on subband dispersion. In both the two-band (HH,LH) and three-band (HH,LH,SO) valence Hamiltonians, the bulk heavy-hole band has a warped dispersion, with the inverse effective mass along the (001) direction given by $m_{\mathrm{HH}}^{*-1}=\gamma_1-2\gamma_2$, while $m_{\mathrm{HH}}^{*-1}=\gamma_1-2\gamma_3$ along the (111) direction. We illustrate how the band warping can, however, be markedly different in the two models along other, lower-symmetry directions, and demonstrate the consequences of this for valence-subband dispersion calculations.

A. Influence of boundary conditions

Figure 6(a) shows the valence-subband dispersion of a 100-Å, $In_xGa_{1-x}AsSb/Al_yGa_{1-y}Sb$ quantum-well structure, calculated using the full four-band Hamiltonian of Eq. (6), with Burt boundary conditions (solid lines) and symmetrized boundary conditions (dashed lines). Figure 6(b) includes the CB, HH, and LH bands (model iii). We find when the lowest conduction band is explicitly included in the calculation that the calculated valence-subband dispersion is always very similar for the two sets of boundary conditions. This is because the lowest conduction band is the dominant remote band contributing to the three-band Luttinger-Kohn valence Hamiltonian. Figures 6(c) and 6(d) show the dispersion calculated using the three-valence-band (HH,LH,SO) and two-valence-band (HH,LH) models, respectively. It is immediately apparent that the dispersion calculated using Burt boundary conditions (solid lines) in Fig. 6(c) is in excellent agreement with that of Fig. 6(a), and likewise when com-

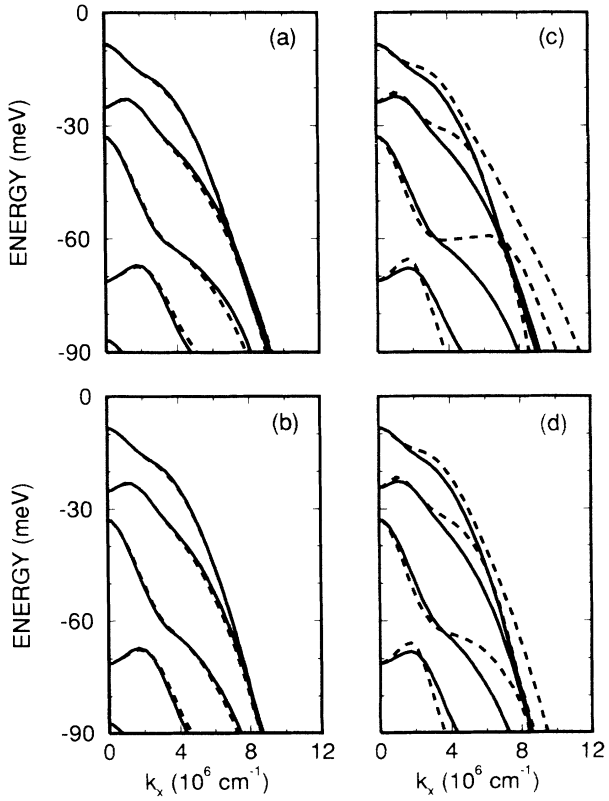

FIG. 6. Valence-subband dispersion of a 100-Å $In_{0.16}Ga_{0.84}As_{0.14}Sb_{0.86}/Al_{0.4}Ga_{0.6}Sb$ quantum well, calculated with the following bands included explicitly in the calculation: (a) CB, HH, LH, and SO; (b) CB, HH, and LH; (c) HH, LH, and SO; and (d) HH and LH only. In each case, solid lines using Burt-Foreman boundary conditions; dotted lines using symmetrized boundary conditions.

paring Figs. 6(d) and 6(b). By contrast, the symmetrized boundary conditions show a much flatter band dispersion in several regions, with the difference being particularly marked around $E = -60$ meV and at larger values of k. Figure 6 thus provides direct confirmation of the correctness of the Burt-Foreman boundary conditions for valence-subband calculations. $Ga_{1-x}In_xAsSb$ is a useful material system to demonstrate the effects of different boundary conditions, as the Luttinger parameters are markedly different in the well and barrier layers (Table I). We would also expect, because of the large spin-orbit splitting, that the calculated subband dispersion should only vary weakly depending on whether the split-off band is included [Fig. 6(c)] or not [Fig. 6(d)] in the calculation. We see that this is indeed the case with Burt-Foreman boundary conditions (solid lines), but that more marked and unintuitive changes occur with the symmetrized boundary conditions (dashed lines).

Figure 7 presents the calculated subband dispersion in a 100-Å $GaAs/Al_{0.2}Ga_{0.8}As$ quantum well. There is a much smaller step in Luttinger parameters between the well and barrier here, and it can be seen that although the Burt boundary conditions give better agreement with the full calculations, the differences are not as marked as in Fig. 6, so that use of the symmetric boundary conditions, although wrong, should be sufficiently accurate for many applications. By contrast, the spin-orbit splitting is approximately halved compared to that in Fig. 6, so we expect a greater difference between the calculations with [Figs. 7(a) and 7(c)] and without [Figs. 7(b) and 7(d)] the SO band included. This is indeed found to be the case. In particular, the inclusion of the SO band makes the highest valence band heavier at large in-plane wave vector, and its dispersion appears to be almost linear between 40 and 140 meV. It can be seen from Figs. 7(a) and 7(b) that this behavior is independent of the boundary conditions used, and must therefore be a consequence of the change in bulk band structure when the split-off band is included.

B. Influence of SO band

Figure 8 shows the valence-subband dispersion along the (10) direction in a 100-Å GaAs/AlAs quantum well, calculated using each of the four band-structure models. The valence-band quantum well is considerably deeper here (644 meV) than in Fig. 7, so we can plot the band dispersion to higher energy. We again see that near the valence-band maximum the Burt boundary conditions in Figs. 8(c) and 8(d) give better agreement with the calculated band structures in Figs. 8(a) and 8(b), respectively. This is no longer the case, however, at higher energies (~ 150 meV and more from the band edge). There are regions at intermediate wave vector in the subband structure of Fig. 8(a) where the dispersion is relatively flat. By

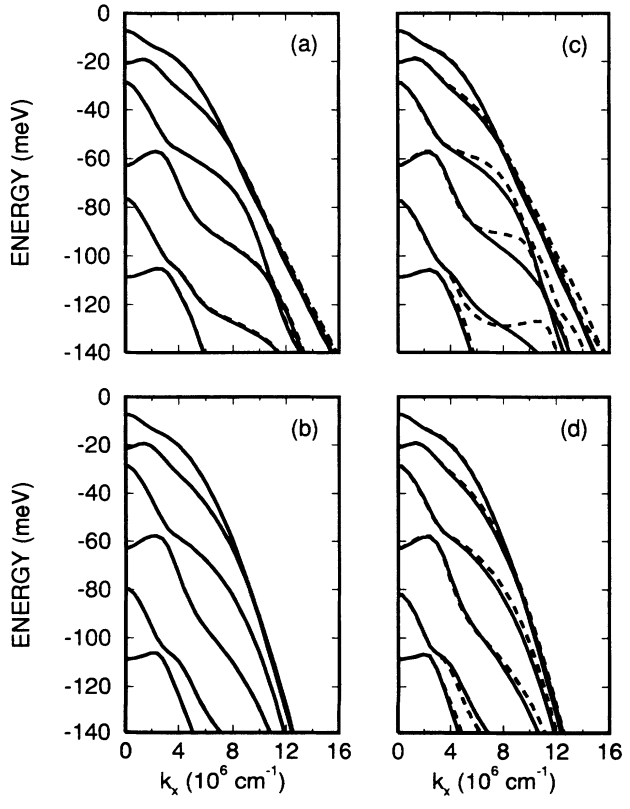

FIG. 7. Valence-subband dispersion of a 100-Å $GaAs/Al_{0.2}Ga_{0.8}As$ quantum well, using the same models and line types as in Fig. 6.

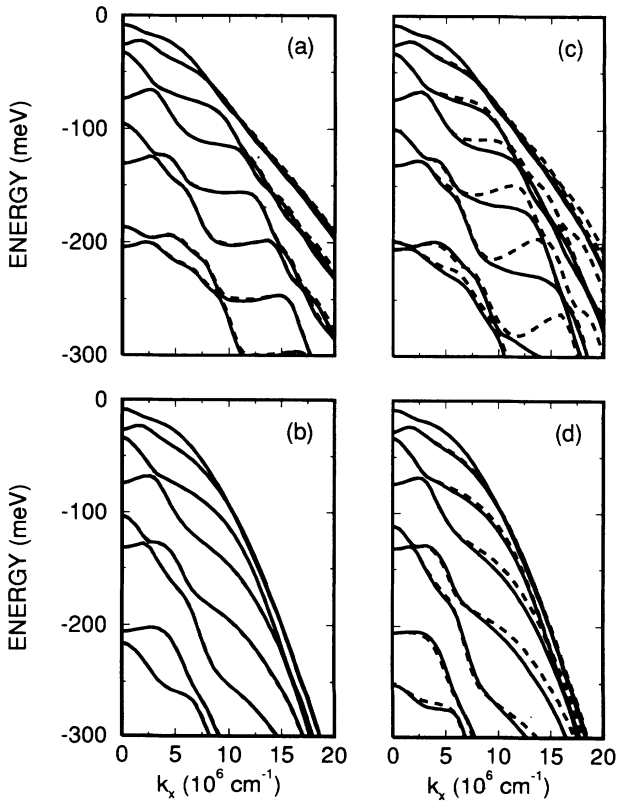

FIG. 8. Valence-subband dispersion of a 100-Å GaAs/AlAs quantum well, using the same models and line types as in Fig. 6.

contrast, the equivalent regions in the band structure of Fig. 8(c) have a downwards dispersion with Burt boundary conditions and an upwards dispersion when symmetrized boundary conditions are used. We attribute this to a breakdown in the assumption that the conduction band can still be treated as a remote band at larger wave vectors and energies.

There is again a marked difference between the calculated band dispersion when the split-off band is included in the calculation [Figs. 8(a) and 8(c)] compared to the cases where it is omitted [Figs. 8(b) and 8(d)]. With the split-off band included, the highest valence bands have a considerably heavier, almost linear, dispersion at large wave vector and, as remarked above, there are also regions with flat or even electronlike dispersion at intermediate wave vector.

We saw earlier how the zone-center confined-state energies in an infinite well of width L can be predicted from the bulk band structure $E(k_z,k_\parallel)$ by taking $k_\parallel=0$ and $k_z=n\pi/L, n=1,2,\ldots$. The situation is more complicated when considering valence-subband dispersion, because of interactions between different subbands, which lead to band mixing effects.[38] It is nevertheless instructive to compare the bulk in-plane band dispersion in different models. We plot the bulk band structure of GaAs as a function of $E(n\pi/L,k_x)$ in Fig. 9, with $L=100$ Å. The main differences found between the subband dispersions of Fig. 8 are also observed here. In particular, the higher bands are heavier at large wave vector k, and electronlike dispersion is also observed at small and intermediate values of k.

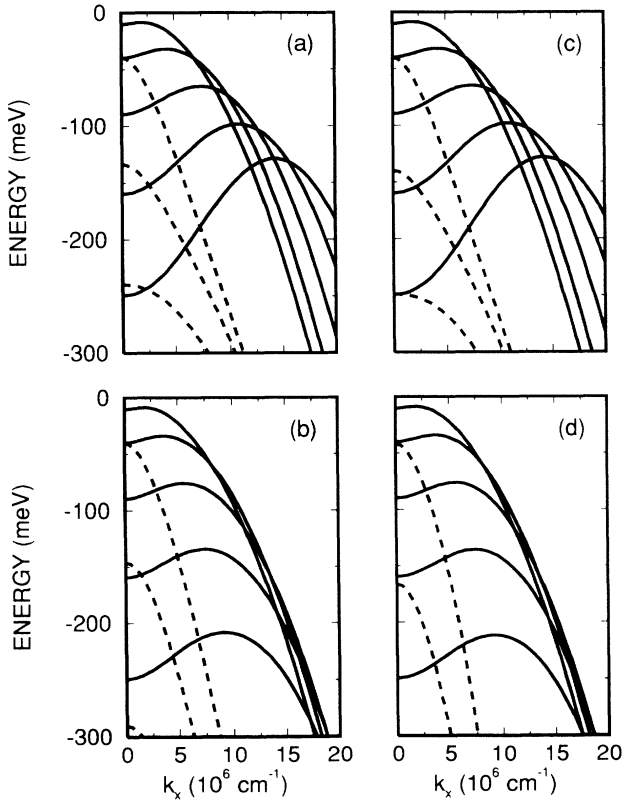

FIG. 9. Valence-band structure of bulk GaAs, calculated along the (100) k_x direction, for fixed values of k_z, namely $k_z=n\pi/(100$ Å), $n=1,2,\ldots$. The following bands are included explicitly in each case: (a) CB, HH, LH, and SO; (b) CB, HH, and LH; (c) HH, LH, and SO; and (d) HH and LH only. It can be seen that the main differences between these bulk band structures are also observed in the 100-Å quantum-well subband structures of Fig. 8. Solid (dotted) lines indicate bulk heavy-hole (light-hole) bands.

The zone-center dispersion of the highest valence band is identical in the two- and three-valence-band models for all directions in the x-y plane at finite k_z. The bulk inverse effective mass in this plane, $m^{-1}_{(001)}$, is given by[33]

$$m^{-1}_{(001)}=\gamma_1+\gamma_2-3\gamma_3^2/\gamma_2 \ . \tag{21}$$

For an isotropic band structure ($\gamma_2=\gamma_3=\gamma_{\rm av}$), the inverse effective mass in Eq. (21) is then equal to the zone-center heavy-hole inverse mass $\gamma_1-2\gamma_{\rm av}$. However, when the band warping is taken into account, Eq. (21) can become negative, and for GaAs is equal to -3.06, using the Luttinger parameters of Table I. We note that this warping of the bulk bands is also responsible for the zone-center electronlike dispersion of the higher heavy-hole subbands in Fig. 8.[42]

The dispersion of the highest valence band in the two- and three-valence-band models is also identical, even to large wave vectors, along the (001) and (111) directions, with the inverse effective masses along the two directions equal to $\gamma_1-2\gamma_2$ and $\gamma_1-2\gamma_3$, respectively. Along other directions, the effective mass is heavier at large k in the three-band compared to the two-band case. This can be seen by comparing the dispersion of the highest hole band in the xz plane in the two-band model and in the three-band model, assuming $\Delta=0$ in the latter case so that a simple analytical expression can be obtained. The dispersion in the two-band model is given by

$$E(k_z,k_x)=-\tfrac{1}{2}\gamma_1 k^2+\sqrt{\gamma_2^2k^4+3(\gamma_3^2-\gamma_2^2)k_x^2k_z^2} \ , \tag{22}$$

while it is given in the three-band case by

$$E(k_z,k_x)=-\tfrac{1}{2}(\gamma_1+\gamma_2)k^2 +\tfrac{3}{2}\sqrt{\gamma_2^2k^4+4(\gamma_3^2-\gamma_2^2)k_x^2k_x^2} \ , \tag{23}$$

where $k^2=k_x^2+k_z^2$. The heavy-hole inverse effective mass along the (101) direction is then, for instance, given by $\gamma_1-(3\gamma_3^2+\gamma_2^2)^{1/2}$ and $\gamma_1+\gamma_2-3\gamma_3$ in the two- and three-band models, respectively. Using the GaAs parameters in Table I, the heavy-hole (101) inverse effective mass is then equal to 1.4 in the two-band case, intermediate between the (001) and (111) values of 2.65 and 1.05, while it is reduced to 0.25 in the three-band case. This enhanced warping in the three-valence-band compared to the two-band case is then responsible for the greater upwards dispersion of the bulk bands in Figs. 9(a) and 9(c), and is the cause of the linear dispersion at large k in Figs. 8(a) and 8(c).

The in-plane warping is often averaged over in QW calculations by applying the axial approximation,[17] which eliminates the angular dependence of the matrix elements

A and B in Eq. (6), by setting the terms involving $\mu=\frac{1}{2}(\gamma_2-\gamma_3)$ to zero. This is equivalent to calculating the band dispersion along the $[\cos(\pi/8),\sin(\pi/8)]$ in-plane direction. This should be a reasonable approximation in the two-valence-band model, as this direction is midway between the (10) and (11) directions, along which the heavy-hole in-plane effective mass is respectively minimized and maximized for large in-plane wave vectors. We see, however, from Figs. 8 and 9 that the in-plane heavy-hole mass along the (10) k_x direction is significantly enhanced in the three-valence-band model, compared to the two-band case, due to the stronger warping in the three-band model. This enhanced warping limits the applicability of the axial approximation using the three-band Hamiltonian.

It is also a cause for concern that the three-band warping is particularly sensitive to the input Luttinger parameters. The GaAs values in Table I were taken from Landolt-Börnstein.[40] If we had used more recently published γ values ($\gamma_1=6.78$, $\gamma_2=1.92$, and $\gamma_3=2.70$),[43,44] these would change $m_{\mathrm{LH}}(001)$, $m_{\mathrm{HH}}(001)$, and $m_{\mathrm{HH}}(111)$ by factors of 5, 10, and 30%, respectively. However, the value of $\gamma_1+\gamma_2-3\gamma_3$, which can be regarded as a measure of the three-band warping, is increased from a value of 0.25 to 0.60, i.e., by 140%. The (01) band dispersion at intermediate and large wave vectors k will then be modified, and the difference between Figs. 9(a) and 9(b) would be reduced.

The band structure in Fig. 8 was calculated for a 100-Å unstrained quantum well. Figure 9 shows how the band warping increases with k_z. The effects of warping on subband dispersion should therefore become more pronounced as the well width L_z is reduced, as the wave vector k_z selected increases with decreasing well width approximately as $k_z\sim\pi/L_z$. Strain also influences the warping: tensile strain increases its effect near the valence-band maximum, while compressive strain reduces it. The warping also increases as the spin-orbit splitting Δ_0 is reduced.

We suggest that a comparative plot such as Fig. 9 should serve as an adequate guide in selecting the Hamiltonian model required for a specific problem. We reiterate, however, that the band warping calculated including the spin-split-off band is strongly sensitive to a combination of the Luttinger parameters which is generally poorly known, namely $\gamma_1+\gamma_2-3\gamma_3$. This is a problem particularly in phosphide-based material systems, such as $Ga_{1-x}In_xP/(Al_yGa_{1-y})_{0.5}In_{0.5}P$, which is of interest for visible laser applications[45] and where the spin-orbit splitting is only of order 100 meV. It may also be of importance in tensile-strained arsenide-based materials, such as $In_x(Ga_yAl_{1-y})_{1-x}As$ structures grown on InP with $x<0.53$, because tensile strain enhances band warping effects near the valence-band maximum. More experimental effort is required to establish accurately the Luttinger parameters for valence-band modeling.

VI. SUMMARY AND CONCLUSIONS

We have investigated the application of the envelope-function method to calculate confinement energies in quantum-well structures, demonstrating how the accuracy both of the calculated zone-center confinement energies and also subband dispersion can be predicted by plotting the equivalent bulk band structure under various approximations.

The effects of band nonparabolicity on zone-center confined-state energy can be predicted directly from the bulk band structure in an infinitely deep quantum well. For finite quantum wells, we first showed how the elimination of spurious solutions from the envelope-function band structure leads to a slightly modified form of the standard result through which the conduction-band confined-state energies are calculated using a one-band model, with an energy-dependent effective mass. We then presented numerical results and arguments based on the one-band model to show how the effects of nonparabolicity on confined-state energies in finite wells can also be predicted directly from the bulk band structure, particularly for the higher confined states, with the difference in calculated confinement energies approaching the difference in the bulk band structures at given wave vector k_z.

There continues to be controversy concerning the correct choice of boundary conditions to describe the continuity of the envelope function across an interface in valence-subband calculations. The most widely used approach has assumed a "symmetrized" form of the Hamiltonian. More recent work by Burt and Foreman based on an exact derivation of envelope-function theory has led to revised boundary conditions. We have settled this issue here by comparing the valence-band structure calculated with the lowest conduction band included either explicitly or treated as a remote band, using perturbation theory. Our results demonstrated that the Burt boundary conditions consistently give the more physically plausible results.

Finally, we compared the valence-subband structure calculated along the (01) direction using the 4×4 and 6×6 Luttinger-Kohn Hamiltonians. For $GaAs/Al_xGa_{1-x}As$ quantum wells we found marked differences between the band structures calculated using the two methods for energies about 100 meV or more from the band edge. This difference arises because the warping of the bulk valence bands increases significantly at intermediate wave vectors when the spin-split-off band is included in the Hamiltonian. This additional warping will influence the band structure at even smaller wave vectors in phosphide-based alloys, such as $Ga_{1-x}In_xP$, where the spin-orbit splitting is only of order 100 meV. The use of the axial model to calculate quantum-well valence-band density of states is therefore questionable in materials with a small spin-orbit splitting. The magnitude of the additional warping in the 6×6 Hamiltonian is very sensitive to the values of the Luttinger parameters used, indicating the importance of investing more effort to determine these parameters accurately.

ACKNOWLEDGMENTS

The authors are grateful to W. Batty and A. Schönfelder for useful discussions concerning this work.

It is a pleasure also to thank J. D. Ralston for his support and encouragement, and for a critical reading of the manuscript. Part of this work has been financially supported by the European Union under ESPRIT Contract No. 6134 (HIRED). E.P.O'R. gratefully acknowledges financial support from the Alexander-von-Humboldt-Stiftung (Bonn, Germany), and B.G. support from the Turkish government.

*On leave from Department of Physics, University of Surrey, Guildford GU2 5XH, U.K.

[1]G. Bastard, *Wave Mechanics Applied to Semiconductor Heterostructures* (Halstead, New York, 1988).

[2]G. Bastard, J. A. Brum, and R. Ferreira, in *Solid State Physics,* edited by D. Turnbull and H. Ehrenreich (Academic, New York, 1991), Vol. 44, p. 229.

[3]M. Altarelli, in *Heterojunctions and Semiconductor Superlattices,* edited by G. Allan, G. Bastard, N. Boccara, M. Lannoo, and M. Voos (Springer, Berlin, 1986), p. 12.

[4]M. G. Burt, J. Phys. Condens. Matter **4**, 6651 (1992).

[5]R. Winkler and U. Rössler, Phys. Rev. B **48**, 8918 (1993).

[6]M. F. H. Schuurmans and G. W. 't Hooft, Phys. Rev. B **31**, 8041 (1985).

[7]W. Pötz, W. Porod, and D. K. Ferry, Phys. Rev. B **32**, 3868 (1985).

[8]R. Eppenga, M. F. Schuurmans, and S. Colak, Phys. Rev. B **36**, 1554 (1987).

[9]L. R. Ram-Mohan, K. H. Yoo, and R. L. Aggarwal, Phys. Rev. B **38**, 6151 (1988).

[10]K. H. Yoo, L. R. Ram-Mohan, and D. F. Nelson, Phys. Rev. B **39**, 12 808 (1989).

[11]A. M. Cohen and G. E. Marques, Phys. Rev. B **41**, 10 608 (1990).

[12]K. J. Duff and K. C. Hass, Surf. Sci. **228**, 479 (1990).

[13]B. Chen, M. Lazzouni, and L. R. Ram-Mohan, Phys. Rev. B **45**, 1204 (1992).

[14]U. Ekenberg, W. Batty, and E. P. O'Reilly, J. Phys. (Paris) Colloq. **48**, C5-553 (1987).

[15]R. Wessel and M. Altarelli, Phys. Rev. B **40**, 12 457 (1989).

[16]C. Y. Chao and S. L. Chuang, Phys. Rev. B **46**, 4110 (1992).

[17]M. Altarelli, U. Ekenberg, and A. Fasolino, Phys. Rev. B **32**, 5138 (1985).

[18]G. D. Saunders and Y. C. Chuang, Phys. Rev. B **31**, 6892 (1985).

[19]D. A. Broido and L. J. Sham, Phys. Rev. B **31**, 883 (1985); **34**, 3917 (1986).

[20]L. C. Andreani, A. Pasquarello, and F. Bassani, Phys. Rev. B **36**, 5887 (1987).

[21]B. Zhu and K. Huang, Phys. Rev. B **36**, 8102 (1987).

[22]W. Batty, U. Ekenberg, A. Ghiti, and E. P. O'Reilly, Semicond. Sci. Technol. **4**, 904 (1989).

[23]G. Bastard, Phys. Rev. B **24**, 5693 (1981); **25**, 7584 (1982).

[24]G. C. LaRocca and M. Cardona, Phys. Status Solidi B **167**, 115 (1991).

[25]B. R. Nag, Appl. Phys. Lett. **59**, 1620 (1991).

[26]R. P. Leavitt, Phys. Rev. B **44**, 11 270 (1991).

[27]M. G. Burt, Appl. Phys. Lett. **65**, 717 (1994).

[28]M. Altarelli, Phys. Rev. B **28**, 842 (1983).

[29]R. A. Morrow and K. R. Brownstein, Phys. Rev. B **30**, 678 (1984); R. A. Morrow, *ibid.* **35**, 8074 (1987).

[30]G. Paasch, P. H. Nguyen, and G. Gobsch, Phys. Status Solidi B **167**, 581 (1990).

[31]S. Nojima, Jpn. J. Appl. Phys. **31**, L1401 (1992).

[32]A. Brezini and M. Sebbani, Phys. Status Solidi B **178**, 141 (1993).

[33]B. A. Foreman, Phys. Rev. B **48**, 4964 (1993); **49**, 1757 (1994).

[34]E. O. Kane, in *Handbook on Semiconductors,* edited by W. Paul (North-Holland, Amsterdam, 1982), Vol. 1, p. 193.

[35]C. R. Pidgeon and R. N. Brown, Phys. Rev. **146**, 575 (1966).

[36]C. G. van de Walle, Phys. Rev. B **39**, 1871 (1989).

[37]P. von Allmen, Phys. Rev. B **46**, 15 376 (1992).

[38]E. P. O'Reilly, Semicond. Sci. Technol. **4**, 121 (1989).

[39]D. F. Nelson, R. C. Miller, and D. A. Kleinman, Phys. Rev. B **35**, 7770 (1987).

[40]*Numerical Data and Functional Relationships in Science and* Technology, edited by O. Madelung, Landolt-Bornstein, New Series, Group III, Vol. 17, Pt. a (Springer-Verlag, New York, 1982).

[41]M. C. P. M. Krijn, Semicond. Sci. Technol. **6**, 27 (1991).

[42]The zone-center effective mass of the nth heavy-hole subband, $m_{\|}$, in an infinite square well, is shown by Foreman [Ref. 33, Eq. (51)] to be equal to

$$m_{\|}^{-1} = m_{(001)}^{-1} + \frac{3\gamma_3^2}{n\pi\gamma_2^2}\sqrt{\gamma_1^2-4\gamma_2^2} \times \cot[\sqrt{(\gamma_1-2\gamma_2)/(\gamma_1+2\gamma_2)}\,n\pi/2] ,$$

where the second term describes the mixing interaction with neighboring light-hole bands of opposite parity. Near the valence-band maximum, the second term makes a significant contribution to $m_{\|}$, both because n is small and also because the angle θ in the cot term is initially small. With increasing subband index n, the magnitude of the second term will tend to decrease, and the zone-center mass will then tend to approach the equivalent bulk value.

[43]L. W. Molenkamp, R. Eppenga, G. W. 't Hooft, P. Dawson, C. T. Foxon, and K. Moore, Phys. Rev. B **38**, 4314 (1988).

[44]B. V. Shanabrook, O. J. Glembocki, D. A. Broido, and W. I. Wang, Superlatt. Microstruct. **5**, 503 (1989).

[45]D. P. Bour, in *Quantum Well Lasers,* edited by P. S. Zory (Academic, New York, 1993), Chap. 9, p. 415.